

RESEARCH ARTICLE

# Label-free pathology by spectrally sliced femtosecond stimulated Raman scattering (SRS) microscopy

Andrew Francis, Kyla Berry, Yikai Chen, Benjamin Figueroa, Dan Fu\*

Department of Chemistry, University of Washington, Seattle, Washington, United States of America

\* [danfu@uw.edu](mailto:danfu@uw.edu)

## Abstract

Optical “virtual biopsy” is an attractive way to improve disease diagnosis and surgical guidance. Many optical microscopy techniques have been developed to provide diagnostic information without the need for tissue sectioning or staining. Among these techniques, label-free chemical imaging is the most desirable. Recently, it has been shown that narrowband, picosecond stimulated Raman scattering (SRS) can achieve comparable morphological contrast to hematoxylin and eosin staining (H&E staining), the ‘gold standard’ of pathology. However, to translate the technique from the bench to the bedside, optimal laser sources and parameters have yet to be identified. Here we describe an improvement to the narrowband SRS microscopy techniques for label-free tissue imaging. Through spectral slicing of broadband, femtosecond pulses, we are able to maintain the same protein/lipid contrast as narrowband SRS while achieving a higher signal-to-noise ratio (SNR). Our method draws upon the benefits of femtosecond pulses (e.g. higher peak power) while preserving those of picosecond pulses (e.g. adequate spectral resolution). We demonstrate this achievement through protein/lipid signal and contrast quantification of mouse brain tissue as a function of bandwidth, and comparison with numerical simulations. Further method validation is provided through imaging of additional mouse tissues: liver, kidney, and skin.



## OPEN ACCESS

**Citation:** Francis A, Berry K, Chen Y, Figueroa B, Fu D (2017) Label-free pathology by spectrally sliced femtosecond stimulated Raman scattering (SRS) microscopy. PLoS ONE 12(5): e0178750. <https://doi.org/10.1371/journal.pone.0178750>

**Editor:** Irene Georgakoudi, Tufts University, UNITED STATES

**Received:** December 29, 2016

**Accepted:** May 18, 2017

**Published:** May 31, 2017

**Copyright:** © 2017 Francis et al. This is an open access article distributed under the terms of the [Creative Commons Attribution License](https://creativecommons.org/licenses/by/4.0/), which permits unrestricted use, distribution, and reproduction in any medium, provided the original author and source are credited.

**Data Availability Statement:** All relevant data are within the paper and its Supporting Information file.

**Funding:** The authors received no specific funding for this work.

**Competing interests:** The authors have declared that no competing interests exist.

## Introduction

Since its discovery over a hundred years ago, hematoxylin and eosin staining (H&E staining) has long served as the ‘gold standard’ of histopathology for achieving strong visual contrast between various cellular features [1]. This contrast is achieved via chemical labelling of specific functional groups present throughout the tissue giving rise to spatial-chemical distribution maps of the tissue. Exploiting key chemical differences between healthy and diseased cells, pathologists can use cellular morphology to not only diagnose the disease but the severity of the condition as well from such staining [2]. While H&E staining is not likely to be replaced by any current technologies, the requirement of tissue excision, sectioning, and staining severely limits its use in an intraoperative setting. Quick and accurate diagnosis is crucial for effective surgical treatment of a variety of cancers including brain, breast, prostate, etc., in which any

residual tumor will increase the risk of cancer relapse. Therefore, a real-time assessment of histopathological features of either excised tumor tissue or the surgical cavity may significantly improve the outcome of the patient [3].

Several competing optical techniques have been developed to address the challenge of intraoperative tissue assessment. One powerful tool is optical coherence tomography (OCT), a low-coherence interferometric technique that images tissue structure at high resolution based on variations in refractive index [4–6]. *In vivo* OCT was initially developed for ophthalmology, but has been rapidly extended to epidermal, cervical, esophageal, and gastrointestinal tissues [7]. Most recently, it has been used for detection of brain tumor infiltration [8]. OCT has a relatively large penetration depth of 1–3 mm, compared to other optical microscopy techniques. However, it suffers from a lack of chemical specificity and thus is unable to provide detailed cellular morphology.

In order to gain chemical contrast, many groups have worked to use autofluorescence and fluorescent staining coupled with confocal or multiphoton microscopy to visualize cellular structures. Although more chemically specific than OCT, both confocal and multiphoton fluorescence are still limited in contrasts: only a few native *in vivo* species are known to autofluoresce, most notably collagen. For tissues that lack strong autofluorescence, an exogenous agent is added to promote strong fluorescent contrast. The two main staining methods are 5-aminolevulinic acid (5-ALA)-induced protoporphyrin IX and nuclear staining, commonly achieved using acridine orange. With nuclear staining, both confocal and multiphoton microscopies have been demonstrated to provide cellular contrasts similar to H&E that enables rapid *ex vivo* assessment of tumor margins. [9,10]. The use of fluorescent dyes does not preclude fluorescence microscopy from *in vivo* imaging, as demonstrated by 5-ALA stained, fluorescence-guided resection surgeries [11–14], but does present additional avenues of intrasample and intersample discrepancies. Dye-based methods suffer from drawbacks including heterogeneous delivery, nonspecific staining, and FDA approval limitations [15].

Stimulated Raman scattering (SRS) microscopy is an emerging analytical, label-free technique that has demonstrated exceptional *ex vivo* [16–20] and *in vivo* [19, 20] tissue imaging capabilities. Compared with fluorescence, it provides specific chemical contrasts without the need for staining. Raman scattering is the inelastic collision between an incident photon and a molecule. The transfer of energy excites a vibrational mode unique to that molecule, making Raman scattering highly qualified to study inhomogeneous systems such as biological tissues. The advent of coherent Raman scattering microscopy addressed the major limitation of applying Raman scattering to tissue imaging—the data acquisition speed. Coherent Raman scattering, including both coherent anti-Stokes Raman scattering (CARS) and SRS, improves the feeble spontaneous Raman scattering effect by a few orders of magnitude, allowing rapid image acquisition at a speed up to video-rate [21]. Traditionally, SRS is achieved using narrowband, picosecond pulses tuned to a particular Raman transition that has a resonance frequency  $\Omega$  equal to the frequency difference between the pump and the Stokes laser  $\omega_p - \omega_s$  [22]. The most commonly used laser system is neodymium based oscillator and a synchronously pumped optical parametric oscillator. The spectral resolution of SRS imaging is determined by the bandwidths of the picosecond lasers, which are typically less than  $10 \text{ cm}^{-1}$ . In order to open SRS up to multi-band excitation, many groups began experimenting with broadband, femtosecond pulses. Multi-band excitation has been reported via frequency tuning [20], multiplexing [23, 24] and spectral focusing [25]. These studies paved the way for broadband, femtosecond SRS as an alternative to the traditional narrowband, picosecond SRS.

Recently, the viability of narrowband, picosecond SRS imaging of brain tumor margins with both frozen and fresh tissue as an alternative to H&E staining has been demonstrated [17, 18, 26]. In the work reported by Ji et al. [17, 18], two-color SRS was adopted to acquire

additional spectroscopic information, allowing for differentiation of various biochemical and morphological features. For biological samples, the two Raman transitions used are typically near 2845 and 2930  $\text{cm}^{-1}$  for lipids and proteins, respectively. In the study conducted by Lu et al. [26], three-color SRS was employed, where the third channel probed corresponds to hemoglobin. While the work reported by Ji et al. and Lu et al. demonstrates the powerful capabilities of their respective systems, the lasers they used have 7 ps long pulses, which suffer from low peak intensity and require high laser power for imaging. Since SRS signal scales with peak intensity, theory posits that spectrally broader, temporally shorter pulses provide higher signal-to-noise ratio (SNR) at the same optical power than narrowband, picosecond pulses. One notable study, conducted by Freudiger et al., detailed the improvement in SNR using spectrally broader, temporally shorter 2 ps pulses through a fiber-based SRS set up [27]. However, fiber-based set ups are limited by their own shortcomings, including high frequency laser noise and difficulties generating sufficiently high power compared to free-space lasers. Regardless, the work done by Freudiger et al. demonstrated that temporally shortened pulses produce higher SNR. Such a system has been recently used by Orringer for intraoperative histology of unprocessed surgical specimen [28].

One important question that remains unsolved in two-color SRS based histopathology is what the optimal laser pulses for imaging are. In one study, a near 12-fold increase in SNR of lipids SRS was observed when the traditional narrowband, picosecond pulses were replaced with broadband, femtosecond SRS [29]. However, there is no systematic study of the influence of pulse duration on SNR. More importantly, spectral broadening associated with shorter pulses results in loss of spectral resolution. It is questionable that in two-color SRS imaging whether the same cell morphological contrasts can be obtained with broadened pulses. In this manuscript, we present two-color SRS tissue imaging using spectrally sliced broadband, femtosecond pulses to systematically investigate the influence of excitation laser bandwidth on SNR and image contrast. After spectral unmixing, our SRS images can provide visual protein/lipid contrast comparable to narrowband, picosecond SRS, and thus, analogous to H&E staining. Importantly, we find that a linear increase in SNR is achieved with pulse bandwidth increase up to 40  $\text{cm}^{-1}$ , while almost identical two-color contrasts are retained compared to narrowband pulses. The results agree with our numerical simulations. This finding has wide implications for future development of SRS imaging systems for intraoperative tumor margin assessment and early tumor diagnosis.

## Methodology

Our experimental set up used is shown in Fig 1. The spectral slicing process begins with a broadband femtosecond dual beam system (Insight DS+ from Spectra Physics) with an 80 MHz repetition rate. The two outputs are: a fixed output of 1040 nm with an average power of 800 mW and bandwidth of 60  $\text{cm}^{-1}$  and a variable output from 680–1300 nm with an average power of 1.2 W and bandwidth of 150  $\text{cm}^{-1}$ . Immediately following emission from the laser, the Stokes beam is modulated at 10 MHz using an electro-optical modulator (EOM). Next, both pulses, pump and Stokes, are spectrally dispersed by a transmission grating, physically sliced with a slit, and returned through the grating at a lower height than incidence to recollimate. The sliced pulses are then combined at a dichroic mirror and overlapped temporally using a delay line in the pump arm. The resulting beam is sent into a home-built laser scanning microscope. A 40X Nikon water immersion objective (Nikon 40X, NA = 1.25) is used to focus the beams onto the tissue sample. At the focus, the Stokes beam has an average power of 35 mW and the pump has an average power of 40 mW. With a combined power of ~75 mW at the focus, we are imaging with similar optical power as recently reported for *in vivo* imaging of

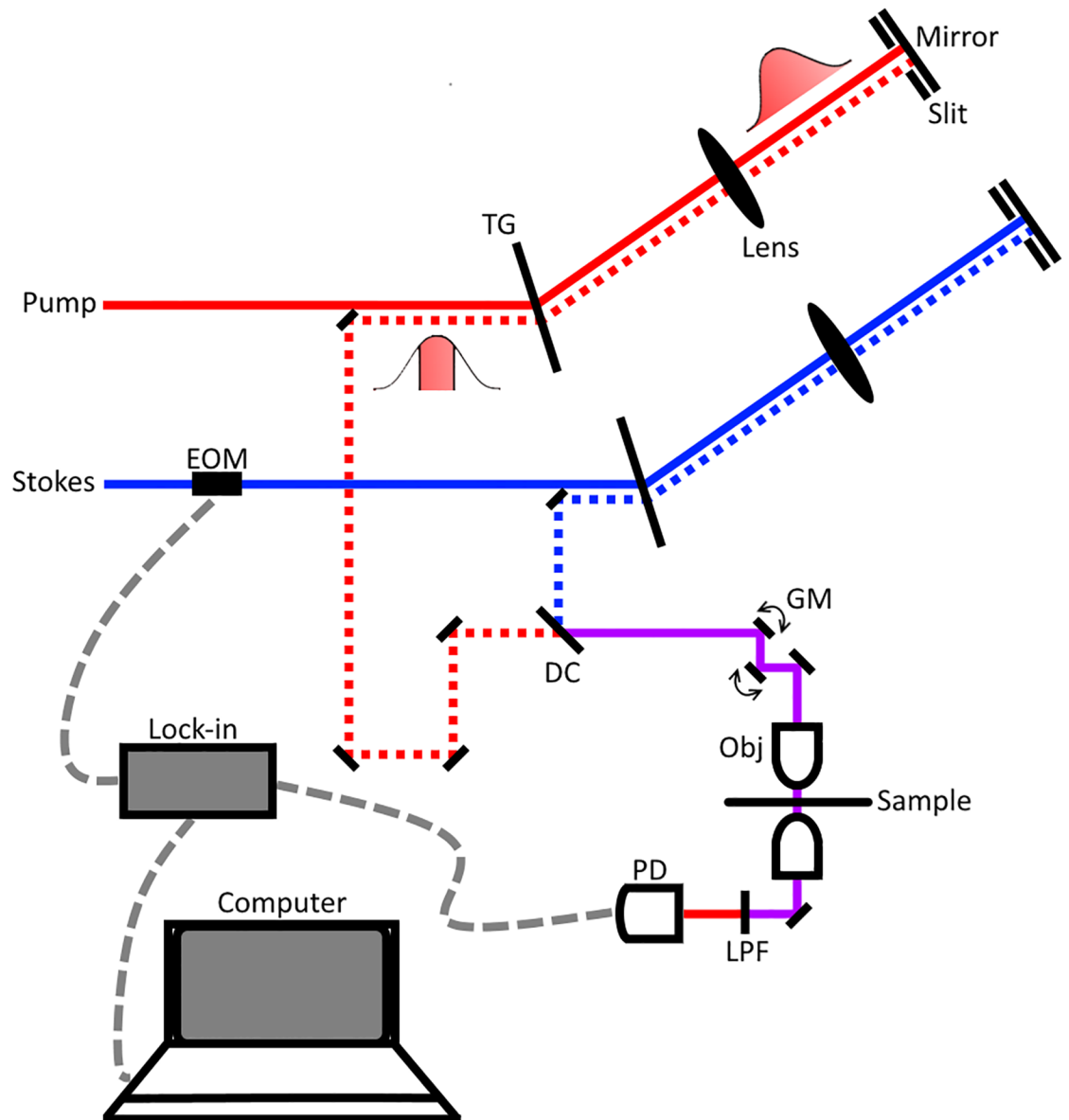


**Fig 1. Experimental spectral slicing set up.** The Stokes laser is modulated by an electro-optical modulator (EOM) at 10 MHz. Pulses are sliced via spectral dispersion through a transmission grating (TG) and a controllable slit placed near the focal point. After slicing, pulses are spatially and temporally synchronized at a dichroic mirror (DC) and directed onto a pair of galvanomirrors (GM). The beams are then sent through the 40x objective, sample, and condenser. Finally, the Stokes beam is filtered out using a low pass filter (LPF) before the beams terminate at the photodiode (PD). Dotted red and blue lines represent an offset in the beam height and the dashed grey lines detail the electrical connections between computer, PD, and lock-in amplifier.

<https://doi.org/10.1371/journal.pone.0178750.g001>

mouse brain vasculature [30], and 2-3-fold less optical power than other ultrafast *ex vivo* multi-photon imaging studies [17, 18, 31]. Moreover, Galli et al observed little to no photodamage of *ex vivo* mouse brain tissue under similar excitation parameters [32]. After passing through the condenser, the Stokes beam is filtered out and the pump reaches a silicon photodiode. Stimulated Raman loss (SRL) signal is detected with a home-built lock-in amplifier [21]. The layout was inspired by work reported by Zhang et al. using a 4-f system to achieve angle-to-

wavelength pulse shaping [33]. Ours differs by adopting a “folded” 4-f system that uses the grating to recollimate the sliced pulses.

Both the pump and Stokes pulses are narrowed using moveable slits that allow for control of bandwidth and central wavelength. The center wavelength and bandwidth of each pulse after slicing were verified using a home-built Michelson interferometer-based spectrometer.

Brain, liver, kidney, and skin tissues were harvested from recently sacrificed mouse carcasses, which were provided by UW Animal Use Training Services (AUTS) according to IACUC protocol 3388–03. The mice (laboratory mice, *mus musculus*) were euthanized by isoflurane or CO<sub>2</sub> overdose and cervical dislocation. The brain was exposed and extracted by removing the scalp and top of the skull. The kidney and liver were collected by making a Y-incision to expose the intestines then clipping the connective tissues. Skin tissues were excised using scissors after hair was removed with Nair. After excision, bulk tissues were placed in phosphate-buffered saline (PBS). Thin sections of tissue were prepared by razor blade sectioning and then placed on a glass slide with additional PBS. To prepare the sample for imaging, a glass coverslip was placed on top to sandwich the tissue specimen between the glass slide and the glass coverslip using double-sided tape as a spacer.

### Results and discussion

We first examined the results of spectral slicing using the aforementioned spectrometer. Fig 2 illustrates the effects of slicing on the Stokes pulse and provides the linear calibration of the slit width. The collected interferograms of the unsliced Stokes pulses are collected and the calculated spectra via Fourier transform (FT) are displayed in Fig 2(a) and 2(b), respectively. As evident by these two figures, the pulses produced by the laser are Gaussian-like in distribution. Spectral slicing induces a convolution of the laser pulse (Gaussian) and the slit (rectangle), shown in Fig 2(c) and 2(d). After slicing, the interferogram more closely represents a sinc function ( $\sin(x)/x$ ), rather than Gaussian. We define the spectral bandwidth as the full width at half maximum (FWHM) in the frequency domain relative to the central wavelength. Fig 2(e) demonstrates the linearity of sliced spectral bandwidth as a function of slit width.

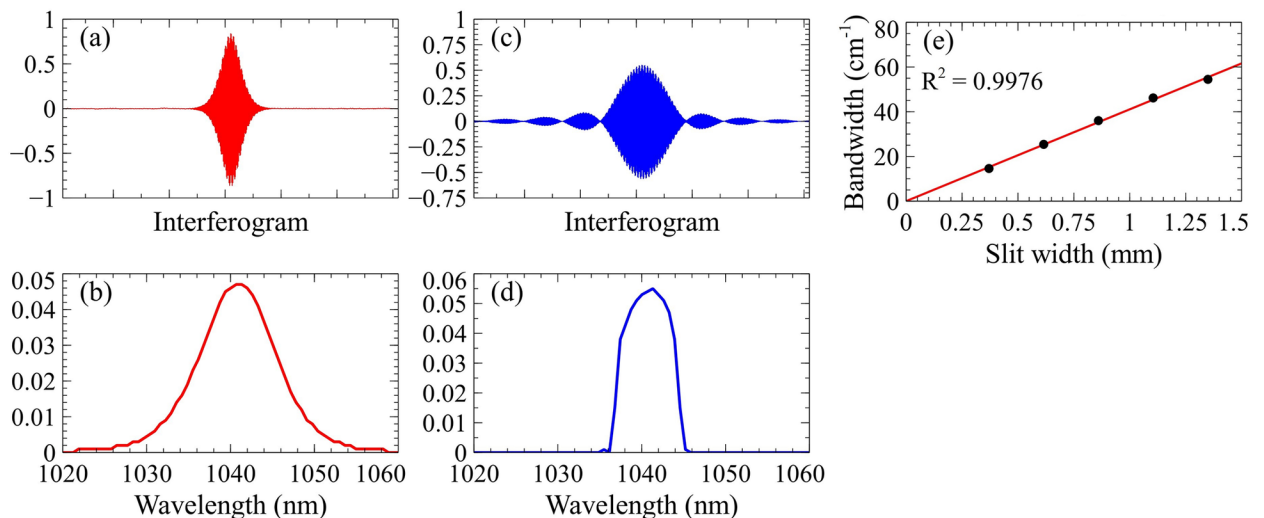


**Fig 2. Effects of slicing on Stokes pulse.** (a) Unsliced interferogram of Stokes pulse using a Michelson interferometer-based spectrometer. (b) Unsliced Stokes frequency profile via Fourier transform (FT) of unsliced interferogram. (c) Sliced interferogram of Stokes pulse. (d) Sliced Stokes frequency profile via FT of sliced interferogram. (e) Linearity of bandwidth as a function of slit width.

<https://doi.org/10.1371/journal.pone.0178750.g002>

The Fourier transform relationship between frequency and time dictates that as a pulse narrows spectrally, it broadens temporally. Therefore, the pulse duration of an unsliced pulse is narrower than that of a sliced pulse. However, the cost of stronger peak intensity is reduced SRS spectral resolution of the selected Raman transition. In [S1 Fig](#), the difference between using narrower ( $10\text{ cm}^{-1}$ ) and broader ( $60\text{ cm}^{-1}$ ) bandwidths is illustrated by highlighting the integration interval difference. Using  $10\text{ cm}^{-1}$  pulses, the  $2855\text{ cm}^{-1}$  channel is predominately lipid signal and the  $2935\text{ cm}^{-1}$  channel is more protein than lipid. When the bandwidth is increased to  $60\text{ cm}^{-1}$  each channel becomes less specific due to higher contributions from the competing chemical (e.g. lipid signal in the  $2935\text{ cm}^{-1}$  channel).

To study this phenomenon, we imaged cross-sections of freshly harvested mouse brain at multiple bandwidths. [Fig 3](#) demonstrates the increase in SNR associated with broadening the pulses from  $10$  to  $40\text{ cm}^{-1}$  at constant excitation power. The images shown have been field normalized to mitigate the field effects caused by the imaging and stitching process. All of the images shown are on the same brightness and contrast scale allowing for a noticeable increase in signal intensity to be clearly observed. Next, the contribution of protein and lipids are unmixed using the same procedures as published by Ji et al. [[18](#)]. This process is achieved by removing the lipid contribution from the protein channel via subtraction. To quantify the contribution of lipids in each channel, we measure the response of oleic acid (representative of cellular lipids) at each bandwidth for both channels. Knowing the contribution at a particular bandwidth for each channel allows us to appropriately scale the protein channel ( $2935\text{ cm}^{-1}$ ) and subtract out the lipid channel ( $2855\text{ cm}^{-1}$ ). [Fig 3](#) provides the unmixed protein (a) and lipid (b) images and the overlay images (c) of mouse brain tissue; the protein channel is shown in blue and the lipid channel, green. The images have been shown at similar brightness and contrast scales to more easily compare the images between bandwidths. Features rich in protein, such as nuclei, appear blue, while features rich in lipids, such as myelin sheaths, appear green. From [Fig 3](#), no apparent changes in contrast are easily observable.

To quantify the variation between the images, the contrast between the two channels for several features was calculated and averaged. We define protein/lipid contrast as the ratio between protein rich nuclei and lipid rich cytoplasm. The results of this analysis and features used are shown in [Fig 4](#).

In [Fig 4](#) three curves are shown demonstrating (b) lipid and protein signal intensity and (c) protein/lipid contrast as a function of bandwidth. [Fig 4\(b\)](#) shows the agreement of experimental findings with our numerical simulation (Matlab 2016, Mathworks) detailing the relationship between SRS signal intensity and bandwidth/pulse duration using a previously derived formula [[34](#)]. Our simulation demonstrates that this relationship is dependent upon the bandwidth of the excitation pulses and the bandwidth of the Raman transition,  $\Gamma$ . More specifically, when excitation pulses are narrower than the Raman transition, the curve is linear; in the opposite case, the curve flattens out and plateaus. For cellular lipids and proteins,  $\Gamma$  is large, which we believe is responsible for the linearity of [Fig 4\(b\)](#). By approximating the Raman transition of proteins and lipids to be  $75$  and  $50\text{ cm}^{-1}$ , respectively, we see that the experimental findings correlate well with the theoretical model. The linear regime of both curves is important because it suggests that optimized excitation conditions exist: inside the linear regime, SNR increases linearly with laser bandwidth; outside the linear regime, the risk of photodamage quickly increases with only marginal increase of SRS signal. [Fig 4\(c\)](#) relates the contrast between the channels to the excitation bandwidth. The trend shows a modest decrease in protein/lipid contrast with increasing bandwidths, with the most substantial being the increase from  $20$  to  $30\text{ cm}^{-1}$ . We believe that this is due to other chemical species present in the sample that are not taken into account in spectral unmixing [[16](#)]. In this study, we only consider the two most prevalent species, proteins and lipids, and neglect contributions from others, most

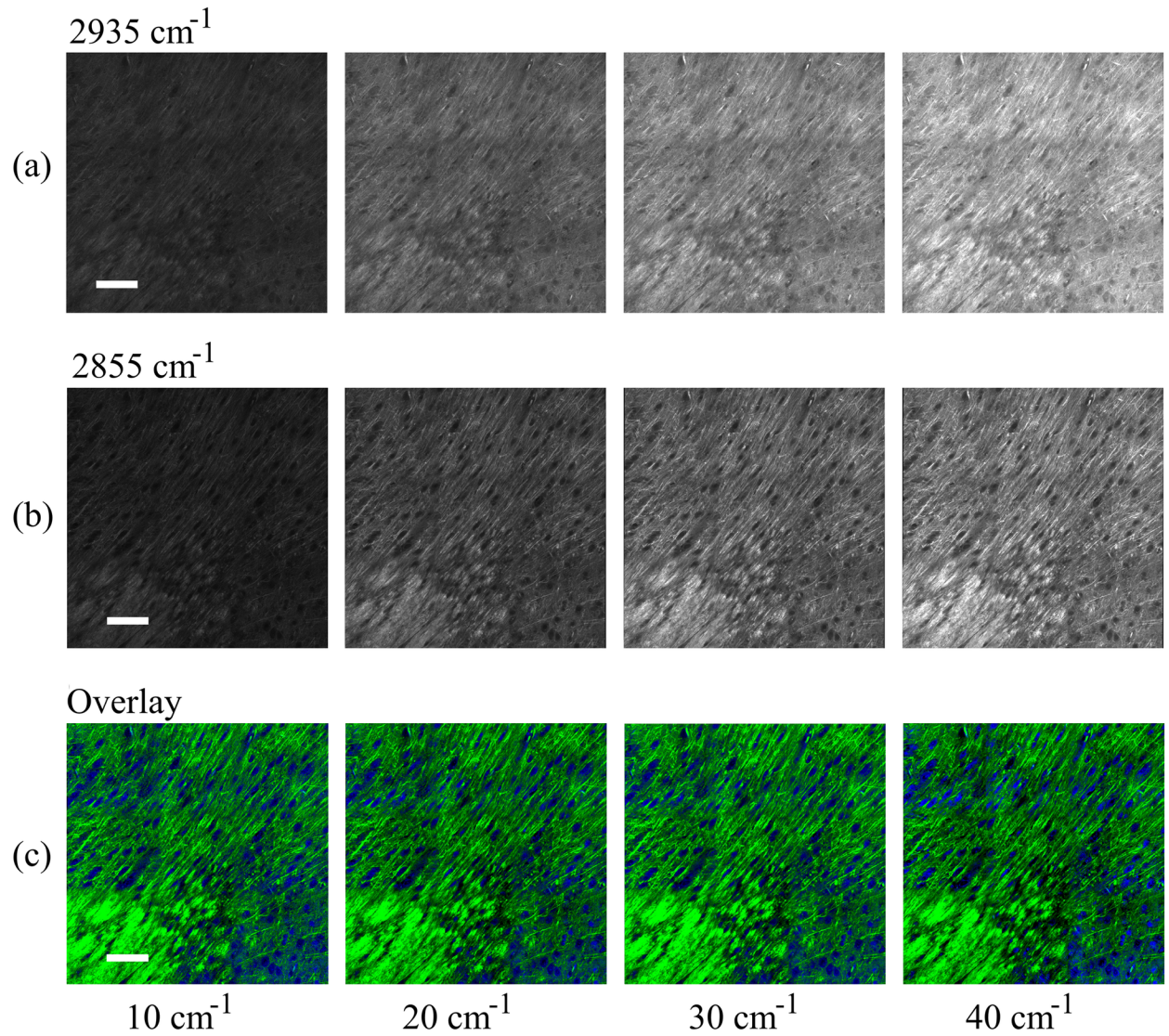


**Fig 3. SRS imaging of mouse brain tissue.** Imaging at (a) 2935  $\text{cm}^{-1}$  (proteins) with bandwidths of 10  $\text{cm}^{-1}$ , 20  $\text{cm}^{-1}$ , 30  $\text{cm}^{-1}$ , and 40  $\text{cm}^{-1}$  from left to right and (b) 2855  $\text{cm}^{-1}$  (lipids) with bandwidths of 10  $\text{cm}^{-1}$ , 20  $\text{cm}^{-1}$ , 30  $\text{cm}^{-1}$ , and 40  $\text{cm}^{-1}$  from left to right. As expected, the mean intensity increases as the bandwidth broadens. After unmixing (subtracting the lipids out of the protein channel) the images are color coded and merged; the proteins are colored blue and the lipids, green. Composite tissue images (c) show only slight differences between 10, 20, 30, and 40  $\text{cm}^{-1}$  from left to right. Scale bar: 100  $\mu\text{m}$ .

<https://doi.org/10.1371/journal.pone.0178750.g003>

notably water and nucleic acids. Water has a very broad band from 2900 to 3600  $\text{cm}^{-1}$  with maxima around 3200 and 3400  $\text{cm}^{-1}$ , and nucleic acids span 2850 to 3100  $\text{cm}^{-1}$  with a maximum near 2955  $\text{cm}^{-1}$ . Therefore, these species will predominantly contribute to the protein channel at 2935  $\text{cm}^{-1}$ , with increasing contribution at larger bandwidth. These contributions confound spectral unmixing and diminish image contrast.

To verify our system's capabilities on a variety of biochemical compositions, we also imaged three other mouse tissues: liver, kidney, and skin. Fig 5 provides the post-processing overlay images of kidney (a, b), liver (c, d), and skin (e, f) using 40  $\text{cm}^{-1}$  excitation pulses. Fig 5(a), 5(c) and 5(e) all show a large field of view (FOV) and Fig 5(b), 5(d) and 5(f) gives a smaller FOV at the specified location. From these images, it is evident that broadband pulses

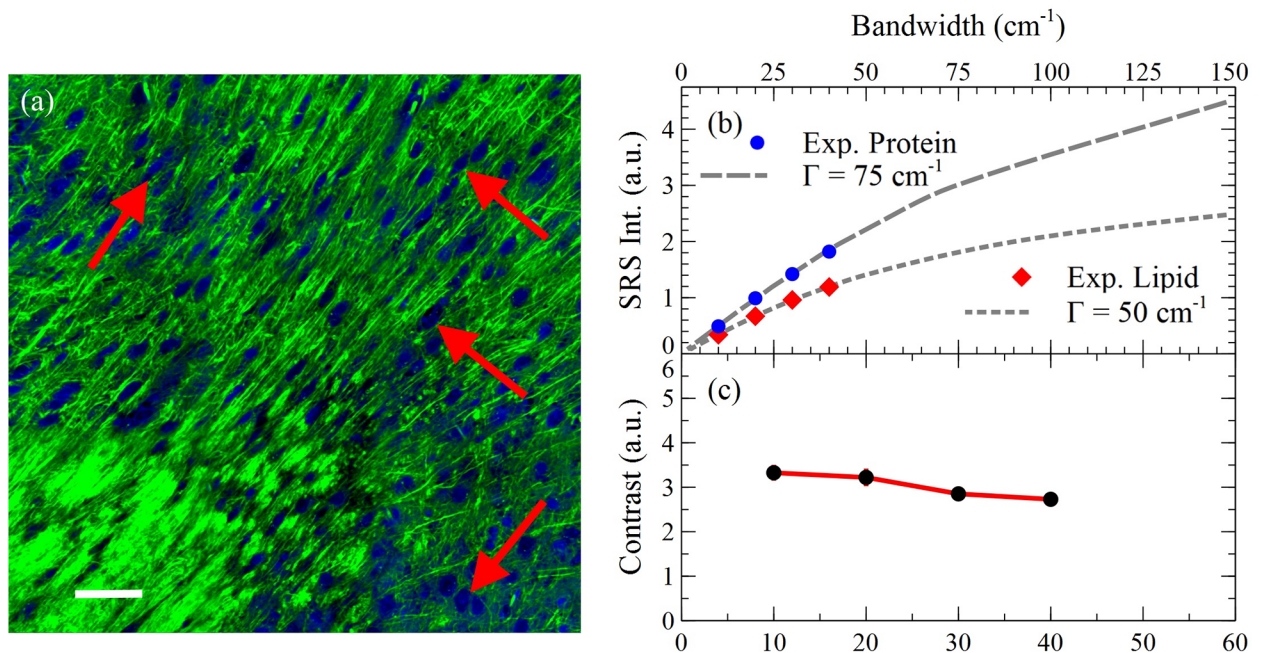


**Fig 4. Signal and contrast dependence on bandwidth.** (a) SRS imaging of mouse brain tissue 30  $\text{cm}^{-1}$  pulses. Total signal for the (b) lipid and protein channels as a function of bandwidth are also shown to illustrate the increase in signal as bandwidth increases. The dashed and dotted gray lines are theoretical curves at 75 and 50  $\text{cm}^{-1}$ , respectively. (c) Contrast at four areas was averaged and plotted as a function of bandwidth. The image shown represents the four areas used and is the overlay at 30  $\text{cm}^{-1}$  from Fig 3 for reference. Scale bar: 200  $\mu\text{m}$ .

<https://doi.org/10.1371/journal.pone.0178750.g004>

are equally effective at providing cellular morphological contrast across a wide range of chemical compositions.

Spectral slicing is a robust method of shaping pulses to very controllable bandwidths/pulse durations; however, a notable disadvantage is the loss of power associated with the physical slicing of the laser beams. One alternative method to pulse shaping is spectral focusing, wherein the excitation pulses are chirped through highly dispersive glass rods [25,35]. In spectral focusing, the Raman transition to be probed is chosen by the temporal delay between the pump and Stokes beams. We used dual-phase lock-in detection that has recently demonstrated by He to perform simultaneous two-color SRS imaging [35]. In our experiment, much shorter pulses were used for imaging. In Fig 6, we provide the results of simultaneous two-channel SRS imaging of freshly excised mouse brain tissue using 30  $\text{cm}^{-1}$  excitation pulses with a combined power of 80 mW at the focus. The two transitions shown are 2850  $\text{cm}^{-1}$  for lipid and 2945  $\text{cm}^{-1}$  for protein excitation. These transitions and bandwidth differ from those used above due to technical differences between spectral slicing and two-channel SRS. Fig 6(a) provides the color scheme used above, while Fig 6(b) remaps the color scheme to a pseudo-H&E color scale [36].

## Conclusion

In summary, the use of spectrally sliced broadband, femtosecond SRS provides similar protein/lipid contrast to narrowband, picosecond SRS after channel unmixing. The main benefit of using broader pulses is increased SNR which is crucial for improving imaging speeds and the limit of detection of SRS. To this extent, we have characterized the relationship between protein/lipid contrast and spectral bandwidth and shown that contrast only decrease slightly

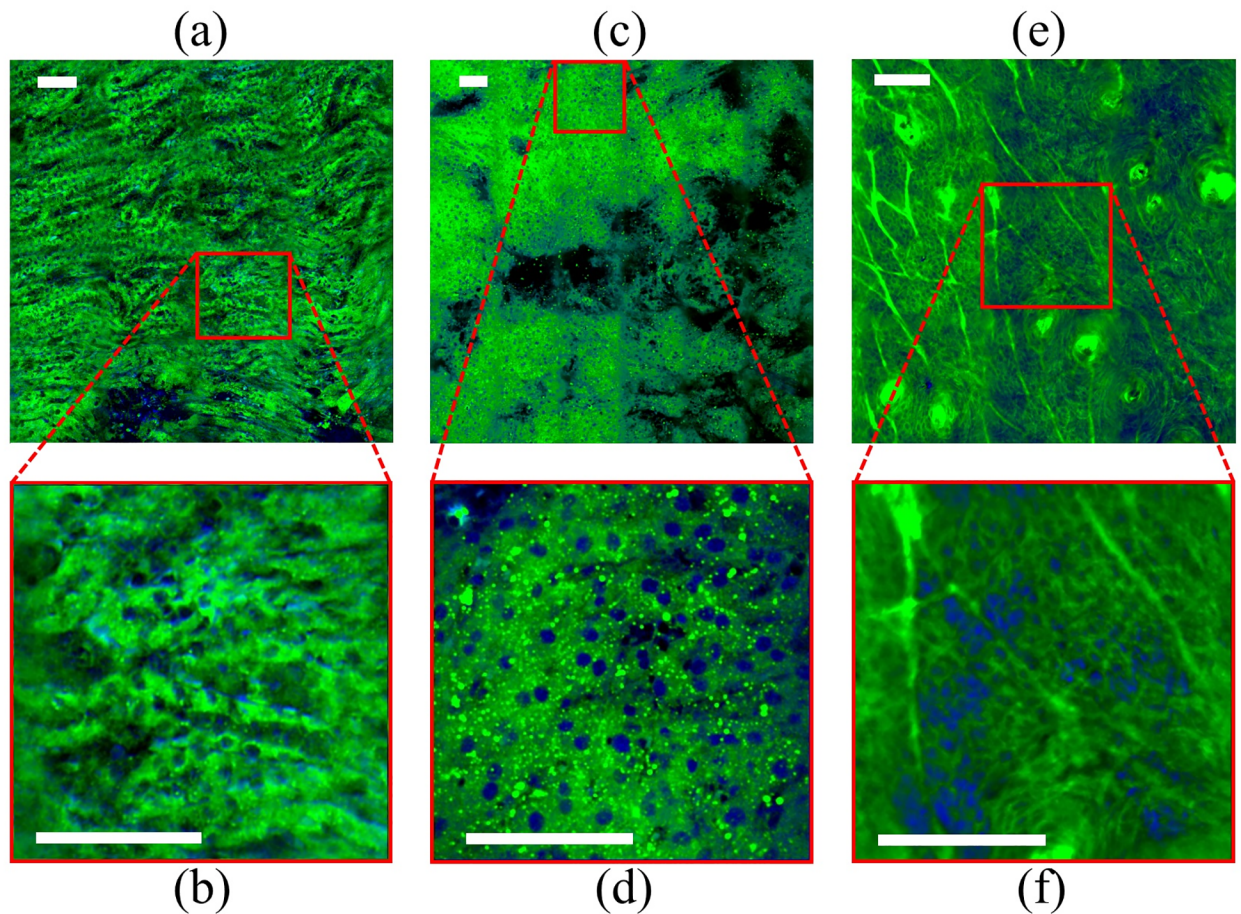


**Fig 5. Broadband, femtosecond SRS imaging of mouse tissue using  $40\text{ cm}^{-1}$  pulses.** The tissues shown are (a, b) kidney, (c, d) liver, and (e, f) skin. For each tissue, the above image is a larger field of view (FOV) and the below image is a smaller FOV indicated by the red outline. After unmixing, the images are color coded and merged; the proteins are colored blue and the lipids, green. Scale bars:  $100\ \mu\text{m}$ .

<https://doi.org/10.1371/journal.pone.0178750.g005>

by going from  $10\text{ cm}^{-1}$  to  $40\text{ cm}^{-1}$ . Moreover, we have demonstrated the optimization of excitation parameters for proteins and lipids within the linear regime between signal intensity and excitation laser bandwidth. We further demonstrated that simultaneous two-color SRS imaging can be achieved with spectral focusing instead of spectral slicing, which more efficiently uses the laser power. The optimal bandwidth for excitation depends on both contrast and photodamage. In previous demonstration of two-color SRS based histopathology [17, 18, 26, 28], 7 ps and 2 ps pulses were used for SRS excitation. It was shown that 2 ps pulses provide better SNR than 7 ps pulses given the same laser power. For transform-limited pulses, 2 ps pulses correspond to  $\sim 5\text{--}10\text{ cm}^{-1}$  laser bandwidth. Our experiment demonstrates that a further 4-fold increase in SNR can be gained by using even shorter pulses without significant loss of morphological contrasts. Although bandwidths larger than  $40\text{ cm}^{-1}$  may still provide contrasts without much degradation, the gain in SNR rapidly decreases due to the limit in Raman transition width of proteins and lipids according to our numerical simulation. Moreover, the photodamage due to high peak power may be of concern at very large laser bandwidth. Our experimental results are promising as a benchmark in two-color SRS based pathology applications. Yet, more work needs to be done regarding broadband, femtosecond SRS. Although we

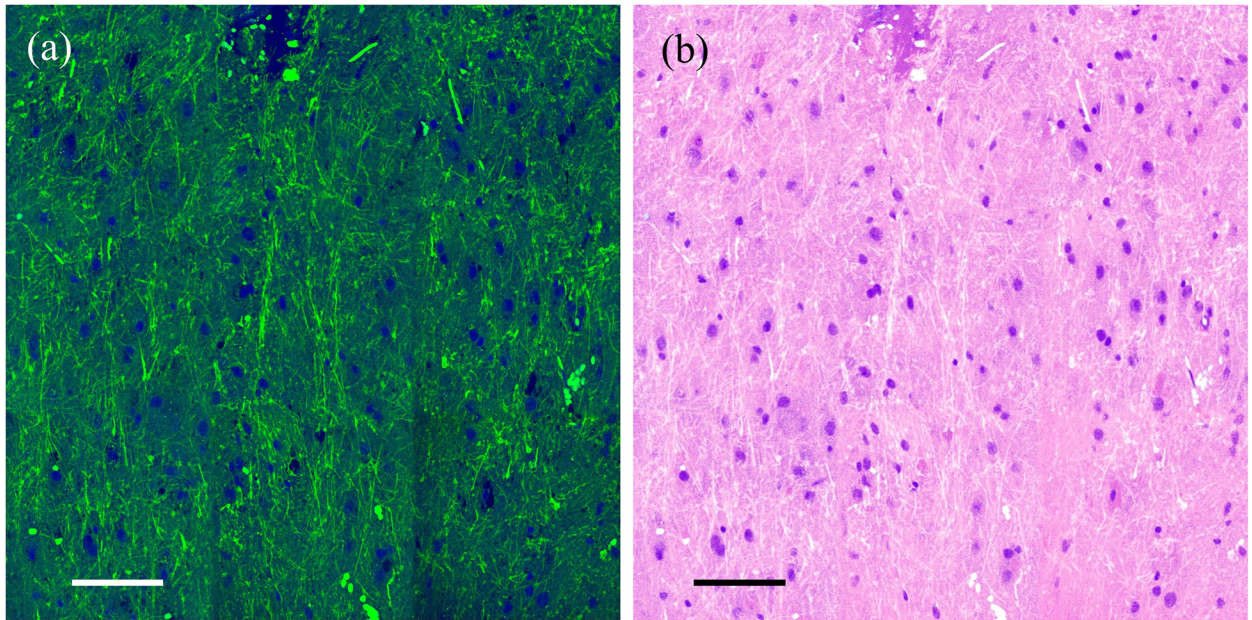


**Fig 6. Simultaneous two-channel SRS imaging of mouse brain tissue using  $30\text{ cm}^{-1}$  pulses.** The mouse brain image shown was collected using dual-phase lock-in detection [32]. (a) Shows the proteins as blue and the lipids, green, while (b) provides a pseudo-H&E color scheme. Scale bars:  $100\text{ }\mu\text{m}$ .

<https://doi.org/10.1371/journal.pone.0178750.g006>

have demonstrated the viability of our system on imaging a wide variety of tissue with varying lipid content, for a more complex tissue environment that contains substantially different biochemical composition or tissue inhomogeneity, our system still needs to be tested. Future work will focus on comparing broadband two-color SRS imaging of human tumor tissues to H&E staining to validate its diagnostic capability.

The benefits demonstrated in this manuscript are essential for the integration of SRS into an intraoperative/guided surgery setting. First, as we, and other groups, have demonstrated, the switch from traditional picosecond excitation lasers to femtosecond lasers is accompanied by significant SNR increase. Theoretically, an order of magnitude increase in SNR is expected for  $40\text{ cm}^{-1}$  broadband pulses compared to the most common  $7\text{ ps}$  laser system given the same incidence power. With higher SNR, less optical power can be used to achieve the same quality of images and imaging speed which mitigates the risk of potential photodamage. Another benefit of broadband, femtosecond SRS is the choice of laser source. In translating from bench to the bedside, fiber laser is poised to play an essential role in clinical imaging. Due to high non-linearity associated with femtosecond pulses, it is often simpler to construct femtosecond lasers compared to picosecond lasers. As a result, more femtosecond lasers are available on the market. Finally, broadband, femtosecond pulses allows simultaneous two-color SRS imaging due to the proximity of the protein and lipid peaks, as demonstrated in this manuscript. Simultaneous two-color SRS offers quicker data acquisition by removing the time required to switch wavelengths, which is necessary for narrowband, picosecond SRS. Furthermore, as demonstrated herein by the results of two-color unmixing, protein/lipid visual contrast is not significantly affected by the bandwidth of the pulses used, within the range of widths detailed. Thus, a carefully optimized broadband, femtosecond system could provide sufficient protein/lipid contrast at significantly higher imaging speed than current narrowband, picosecond two-color SRS.

## Supporting information

**S1 Fig. Dependence of signal amplitude and contrast on bandwidth.** Normalized spontaneous Raman spectra of bovine serum albumin (BSA) and oleic acid are shown as representative of proteins and lipids, respectively. Shown is the difference in excitation of the protein channel ( $2935\text{ cm}^{-1}$ ) and the lipid channel ( $2855\text{ cm}^{-1}$ ) with (a)  $10\text{ cm}^{-1}$  pulses and (b)  $60\text{ cm}^{-1}$  pulses. (TIF)

## Author Contributions

**Conceptualization:** DF AF.

**Data curation:** AF BF.

**Formal analysis:** AF DF.

**Funding acquisition:** DF.

**Investigation:** AF KB YC.

**Methodology:** DF AF.

**Project administration:** DF.

**Resources:** DF.

**Software:** BF DF AF.

**Supervision:** YC DF.

**Validation:** KB AF.

**Visualization:** AF DF.

**Writing – original draft:** AF DF.

**Writing – review & editing:** AF KB YC BF DF.

## References

1. King DK, King LAC. A Brief Historical Note on Staining by Hematoxylin and Eosin. *Am. J. Dermatopath.* 1986; 8(2):168. PMID: [2424331](#)
2. Chan J. The Wonderful Colors of the Hematoxylin-Eosin Stain in Diagnostic Surgical Pathology. *Int. J. Surg. Pathol.* 2014; 22(1):12–32. <https://doi.org/10.1177/1066896913517939> PMID: [24406626](#)
3. Schneider JP, Schulz T, Schmidt F, Dietrich J, Lieberenz S, Trantakis C, et al. Gross-total Surgery of Supratentorial Low-grad Gliomas under Intraoperative MR Guidance. *Am. J. Neuroradiol.* 2001; 22(1):89–98. PMID: [11158893](#)
4. Hariri LP, Mino-Kenudson M, Mark EJ, Suter MJ. In Vivo Optical Coherence Tomography: The Role of the Pathologist. *Arch. Pathol. Lab. Med.* 2012; 136(1):1492–1501.
5. Tearney GJ, Brezinski ME, Bouma BE, Boppart SA, Pitris C, Southern JF, et al. In Vivo Endoscopic Optical Biopsy with Optical Coherence Tomography. *Science* 1997; 276(5321):2037–2039. PMID: [9197265](#)
6. Huang D, Swanson EA, Lin CP, Schuman JS, Stinson WG, Chang W, et al. Optical Coherence Tomography. *Science.* 1991; 254(5035):1178–1181. PMID: [1957169](#)
7. Zysk AM, Nguyen FT, Oldenburg AL, Marks DL, Boppart SA. Optical coherence tomography: a review of clinical development from bench to bedside. 2007; 12(5):051403
8. Kut C, Chaichana KL, Xi J, Raza SM, Ye X, McVeigh ER, et al. Detection of human brain cancer infiltration ex vivo and in vivo using quantitative optical coherence tomography. *Sci. Transl. Med.* 2015; 7(292):100.

9. Tao YK, Shen D, Sheikine Y, Ahsen OO, Wang HH, Schmolze DB, et al. Assessment of breast pathologies using nonlinear microscopy. *P. Natl. A. Sci.* 2014; 111(43):15304–15309.
10. Sanai N, Eschbacher J, Hattendorf G, Coons SW, Preul MC, Smith KA, et al. Intraoperative confocal microscopy for brain tumors: a feasibility analysis in humans. *Neurosurgery.* 2011; 68(1):282–290.
11. Stummer W, Novotny A, Stepp H, Goetz C, Bise K, Reulen HJ. Fluorescence-guided resection of glioblastoma multiforme utilizing 5-ALA-induced porphyrins: a prospective study in 52 consecutive patients. *J. Neurosurg.* 2000; 93(6):1003–1013. <https://doi.org/10.3171/jns.2000.93.6.1003> PMID: 11117842
12. Stummer W, Pichlmeier U, Meinel T, Wiestler OD, Zanella F, Reulen HJ. Fluorescence-guided surgery with 5-aminolevulinic acid for resection of malignant glioma: a randomised controlled multicentre phase III trial. *Lancet Oncol.* 2006; 7(5):392–401. [https://doi.org/10.1016/S1470-2045\(06\)70665-9](https://doi.org/10.1016/S1470-2045(06)70665-9) PMID: 16648043
13. Sanai N, Snyder LA, Honea NJ, Coons SW, Eschbacher JM, Smith KA, et al. Intraoperative confocal microscopy in the visualization of 5-aminolevulinic acid fluorescence in low-grade gliomas. *J. Neurosurg.* 2011; 115(4):740–748. <https://doi.org/10.3171/2011.6.JNS11252> PMID: 21761971
14. Stummer W, Tonn JC, Goetz C, Ullrich W, Stepp H, Bink A, et al. 5-Aminolevulinic Acid-derived Tumor Fluorescence: The Diagnostic Accuracy of Visible Fluorescence Qualities as Corroborated by Spectrometry and Histology and Postoperative Imaging. *Neurosurg.* 2014; 74(3):310–319.
15. Moore GE. Fluorescein as an Agent in the Differentiation of Normal and Malignant Tissues. *Science.* 1947; 106(2745):130–131.
16. Lu FK, Basu S, Igras V, Hoang MP, Ji M, Fu D, et al. Label-free DNA imaging in vivo with stimulated Raman scattering microscopy. *P. Natl. A. Sci.* 2015; 112(37):11624–11629.
17. Ji M, Orringer DA, Freudiger CW, Ramkisson S, Liu X, Lau D, et al. Rapid, Label-Free Detection of Brain Tumors with Stimulated Raman Scattering Microscopy. *Sci. Transl. Med.* 2013; 5(201):119.
18. Ji M, Lewis S, Camelo-Piragua S, Ramkisson SH, Snuderl M, Venneti S, et al. Detection of human brain tumor infiltration with quantitative stimulated Raman scattering microscopy. *Sci. Transl. Med.* 2015; 7(309):163.
19. Freudiger CW, Min W, Saar BG, Lu S, Holtom GR, He C, et al. Label-Free Biomedical Imaging with High Sensitivity by Stimulated Raman Scattering Microscopy. *Science.* 2008; 322(5909):1857–1861. <https://doi.org/10.1126/science.1165758> PMID: 19095943
20. Ozeki Y, Umemura W, Otsuka Y, Satoh S, Hashimoto H, Sumimura K, et al. High-speed molecular spectral imaging of tissue with stimulated Raman scattering. *Nat. Photonics.* 2012; 6(1):845–851.
21. Saar BG, Freudiger CW, Reichman J, Stanley CM, Holtom GR, Xie XS. Video-Rate Molecular Imaging in Vivo with Stimulated Raman Scattering Science. 2010; 330(6009):1368–1370. <https://doi.org/10.1126/science.1197236> PMID: 21127249
22. Cheng JX, Xie XS. *Coherent Raman Scattering Microscopy.* CRC Press; 2013.
23. Fu D, Lu FK, Zhang X, Freudiger CW, Pernik DR, Holtom G, et al. Quantitative Chemical Imaging with Multiplex Stimulated Raman Scattering Microscopy. *J. Am. Chem. Soc.* 2012; 134(8):3623–3626. <https://doi.org/10.1021/ja210081h> PMID: 22316340
24. Liao CS, Wang P, Wang P, Li J, Lee HJ, Eakins G, et al. Spectrometer-free vibrational imaging by retrieving stimulated Raman signal from highly scattered photons. *Sci Adv* 2015; 1(9):1500738.
25. Fu D, Holtom G, Freudiger C, Zhang X, Xie XS. Hyperspectral Imaging with Stimulated Raman Scattering by Chirped Femtosecond Lasers. *J. Phys. Chem. B.* 2013; 117(16):4634–4640. <https://doi.org/10.1021/jp308938t> PMID: 23256635
26. Lu FK, Calligaris D, Olubiyi OI, Norton I, Yang W, Santagata S, et al. Label-Free Neurosurgical Pathology with Stimulated Raman Imaging. *Cancer Res.* 2016; 76(12):3451–3462. <https://doi.org/10.1158/0008-5472.CAN-16-0270> PMID: 27197198
27. Freudiger CW, Yang W, Holtom GR, Peyghambarian N, Xie XS, Kieu KQ. Stimulated Raman scattering microscopy with a robust fibre laser source. *Nat. Photonics.* 2014; 8(1):153–159.
28. Orringer DA, Pandian B, Niknafs YS, Hollon TC, Boyle J, Lewis S, et al. Rapid intraoperative histology of unprocessed surgical specimens via fibre-laser-based stimulated Raman scattering microscopy. *Nature Biomedical Engineering* 2017; 1(1):0027.
29. Zhang D, Slipchenko MN, Cheng JX. Highly Sensitive Vibrational Imaging by Femtosecond Pulse Stimulated Raman Loss. *J. Phys. Chem. Lett.* 2011; 2(11):1248–1253. <https://doi.org/10.1021/jz200516n> PMID: 21731798
30. Kobat D, Durst ME, Nishimura N, Wong AW, Schaffer CB, Xu C. Deep tissue multiphoton microscopy using longer wavelength excitation. *Opt. Express.* 2009; 17(16):13354–13364 PMID: 19654740
31. Paoli J, Smedh M, Wennberg AM, Ericson M. Multiphoton Laser Scanning Microscopy on Non-Melanoma Skin Cancer: Morphologic Features for Future Non-Invasive Diagnostics. *J. Invest. Dermatol.* 2008; 128(11):1248–1255.

32. Galli R, Uckermann O, Andreson EF, Geiger KD, Koch E, Schackert G, et al. Intrinsic Indicator of Photo-damage during Label-Free Multiphoton Microscopy of Cells and Tissues. 2014; 9(10):e1110295.
33. Zhang D, Slipchenko MN, Leaird DE, Weiner AM, Cheng JX. Spectrally modulated stimulated Raman scattering imaging with an angle-to-wavelength pulse shaper. *Opt. Express*. 2013; 21(11):13864–13874. <https://doi.org/10.1364/OE.21.013864> PMID: 23736639
34. Fu D. Developing Novel Nonlinear Optical Contrast for Biomedical Imaging. PhD Thesis, Princeton University. 2009. <https://pulsesearch.princeton.edu/catalog/5642376>
35. He R, Xu Y, Zhang L, Ma S, Wang X, Ye D, et al. Dual-phase stimulated Raman scattering microscopy for real-time two-color imaging. *Optica*. 2017; 4(1):44–47.
36. Gareau DS. Feasibility of digitally stained multimodal confocal mosaics to simulate histopathology. *J Biomed Opt* 2009; 14(3):034050. <https://doi.org/10.1117/1.3149853> PMID: 19566342